

An adaptive multiresolution discontinuous Galerkin method with artificial viscosity for scalar hyperbolic conservation laws in multidimensions

Juntao Huang ^{*} Yingda Cheng [†]

July 2, 2022

Abstract

In this paper, we develop an adaptive multiresolution discontinuous Galerkin (DG) scheme for scalar hyperbolic conservation laws in multidimensions. Compared with previous work for linear hyperbolic equations [25, 26], a class of interpolatory multiwavelets are applied to efficiently compute the nonlinear integrals over elements and edges in DG schemes. The resulting algorithm, therefore can achieve similar computational complexity as the sparse grid DG method for smooth solutions. Theoretical and numerical studies are performed taking into consideration of accuracy and stability with regard to the choice of the interpolatory multiwavelets. Artificial viscosity is added to capture the shock and only acts on the leaf elements taking advantages of the multiresolution representation. Adaptivity is realized by auto error thresholding based on hierarchical surplus. Accuracy and robustness are demonstrated by several numerical tests.

Keywords: discontinuous Galerkin methods; multiresolution analysis; sparse grids; hyperbolic conservation laws; artificial viscosity.

^{*}Department of Mathematics, Michigan State University, East Lansing, MI 48824, USA. E-mail: huangj75@msu.edu.

[†]Department of Mathematics, Department of Computational Mathematics, Science and Engineering, Michigan State University, East Lansing, MI 48824, USA. E-mail: ycheng@msu.edu. Research is supported by NSF grants DMS-1453661 and DMS-1720023.

1 Introduction

In this paper, we develop an adaptive multiresolution discontinuous Galerkin (DG) method for scalar nonlinear conservation laws in multidimensional case:

$$\partial_t u + \nabla \cdot \mathbf{f}(u) = 0, \quad (\mathbf{x}, t) \in \Omega \times (0, T], \quad (1)$$

with appropriate initial and boundary conditions. Here $\Omega \subset \mathbb{R}^d$, $u = u(\mathbf{x}, t)$ is the unknown function, and $\mathbf{f}(u) = (f_1(u), f_2(u), \dots, f_d(u))$ is the physical flux. We assume $\Omega = [0, 1]^d$ in the paper, but the discussion can be easily generalized to arbitrary box-shaped domains.

The DG method is a class of finite element methods using discontinuous approximation space for the numerical solutions and the test functions. The Runge-Kutta DG scheme for hyperbolic equations became very popular due to its provable stability and convergence, excellent conservation properties and accommodation for adaptivity and parallel implementations. We refer readers to the review papers [16, 14] for details. To adapt the degrees of freedom according to the local behavior of the numerical solution, many kinds of *a posteriori* error estimates have been designed for the DG schemes for hyperbolic equations, see e.g. [7, 1, 45, 29, 32, 30]. On the other hand, by using multiresolution analysis (MRA), automatic adaptivity can be achieved and no additional *a posteriori* error indicator is needed. Such ideas have been used to accelerate the computations for conservation laws under finite difference or finite volume frameworks [28, 8, 18, 4, 17, 12] and were used as trouble cell indicators for DG methods [50]. In recent years, there have been interests in developing adaptive multiresolution DG schemes [11, 5]. In particular, multiresolution-based adaptive DG schemes for solving one dimensional scalar conservation laws were proposed by Müller *et al.* in [33] and further extended to multidimensional cases [22], compressible flows [35, 21] and shallow water equations [20, 36].

Another idea to utilize the computational advantages of the MRA framework is called the sparse grid method [10], which is a well-known tool to compute high-dimensional PDEs and stochastic differential equations. Based on the attractive features of DG methods for solving convection-dominated problems, in recent years, we initiated a line of research developing the (adaptive) sparse grid DG methods, including the work for elliptic equations [51], transport equations [25], reaction-diffusion equations [40] and Vlasov-Maxwell equations [48]. For smooth solutions, the schemes we constructed can successfully reduce the number of degrees of freedom (DoF) of unknown

from $\mathcal{O}(h^{-d})$ to $\mathcal{O}(h^{-1}|\log_2 h|^{d-1})$ for d -dimensional problem, where h is the uniform mesh size in each dimension. Stability and conservation of standard DG methods can be maintained. Errors are only slightly deteriorated for smooth solutions. Adaptivity can be incorporated naturally to treat solutions with less smoothness or local structures.

However, the main bottleneck for the sparse grid DG scheme developed so far is that, it is mainly for “*linear*” equations. Here, “*linear*” refers to either linear variable coefficient equations with given coefficients or coefficients that have some specified dependence on the unknowns, e.g. Vlasov systems through self-consistent field. There remain significant challenges to extend the methods to truly nonlinear problems in an efficient manner. For example, previous work in the literature on adaptive multiresolution DG schemes resort to the finest scale for the actual time evolution for the nonlinear terms. Therefore, the computational cost is proportional to the number of cells on the finest level, i.e. $\mathcal{O}(h^{-d})$ operations, and the reduced DoF in the solution representation is not realized in the actual computation. For nonlinear equations, there is only limited literature on collocation or finite difference based sparse grid methods [23], and the order of accuracy of the schemes is low. Sparse grid combination methods work for nonlinear problems, but they are less flexible in terms of adaptivity [39].

The objective of this work is to develop an adaptive multiresolution DG method to solve the nonlinear equation (1) efficiently. We would like to construct a scheme that can recover the computational complexity of the sparse grid method for smooth solutions. To represent a nonlinear function, it is natural to consider interpolation or collocation methods [31, 2]. This is achieved by using sparse grid collocation methods introduced in [49], which gives a framework to design adaptive sparse grid collocation onto arbitrary high order piecewise polynomial spaces. We approximate the nonlinear terms in the semi-discrete DG scheme for (1) by a linear combination of collocation basis functions up to required order of accuracy. We analyze the accuracy of the DG scheme with interpolation following the approach in [13, 34]. We compare different ways of sparse grid collocation methods and find that there exists some *weak* instability for Lagrange interpolation when solving (1). This motivates us to apply Hermite interpolation, which is more stable than the Lagrange interpolation [27]. With the Hermite multiwavelet interpolations, we can obtain satisfactory numerical results which coincide with our local truncation error analysis.

Another challenge we address in the paper is how to capture the shock

and entropy solutions to (1). There are two approaches in the literature. The first one is to apply limiters to control spurious oscillations and at the same time maintain accuracy in smooth regions, e.g., the minmod-type limiter [15], the moment-based limiter [9] and WENO limiter [43]. However, it is quite difficult to impose limiters in the sparse grid DG methods, due to the global feature of the basis functions. Also a preliminary calculation from us shows that the piecewise constant sparse grid DG method in multidimensions is not monotone. This motivates us to use the second approach, which is to add artificial viscosity, see e.g. [6, 42, 24, 37, 38]. The idea is to add a diffusion term in the equation where the diffusion coefficient vanishes in the smooth region and becomes non-zero near the shock. This can be achieved by techniques such as entropy production [24] or local smoothness indicator [42]. We add an artificial viscosity term following the approach in [6]. Based on the estimate of the magnitudes of coefficients of hierarchical basis functions in [25, 26], we propose a smoothness indicator, which is built upon the inherent MRA and can automatically pick out the discontinuous regions. To improve the computational efficiency of our scheme, the implicit-explicit (IMEX) Runge-Kutta time integration is applied, where the nonlinear convection term is treated explicitly and the linear diffusion term is computed implicitly.

The rest of this paper is organized as follows. In Section 2, we review MRA associated with two sets of basis functions, i.e., the Alpert's multiwavelets [3] and the interpolatory multiwavelets [49]. The adaptive multiresolution DG scheme is constructed in Section 3 using both sets of multiwavelets. The numerical performance is validated by linear advection equations, Burgers' equations and KPP problems in Section 4. We conclude the paper in Section 5. The appendix collects the explicit formulas of the interpolatory multiwavelets used in this paper.

2 MRA and multiwavelets

In this section, we review MRA associated with piecewise polynomial space. We will start with Alpert's multiwavelets [3] and then review the interpolatory multiwavelets [49].

2.1 Alpert's multiwavelets

We first review MRA achieved by Alpert's basis functions in one dimension [3]. We define a set of nested grids, where the n -th level grid Ω_n consists of 2^n uniform cells

$$I_n^j = (2^{-n}j, 2^{-n}(j+1)], \quad j = 0, \dots, 2^n - 1$$

for $n \geq 0$. For notational convenience, we also denote $I_{-1} = [0, 1]$. The usual piecewise polynomial space of degree at most $k \geq 1$ on the n -th level grid Ω_n for $n \geq 0$ is denoted by

$$V_n^k := \{v : v \in P^k(I_n^j), \forall j = 0, \dots, 2^n - 1\}. \quad (2)$$

Then, we have the nested structure

$$V_0^k \subset V_1^k \subset V_2^k \subset V_3^k \subset \dots$$

We can now define the multiwavelet subspace W_n^k , $n = 1, 2, \dots$ as the orthogonal complement of V_{n-1}^k in V_n^k with respect to the L^2 inner product on $[0, 1]$, i.e.,

$$V_{n-1}^k \oplus W_n^k = V_n^k, \quad W_n^k \perp V_{n-1}^k.$$

For notational convenience, we let $W_0^k := V_0^k$, which is the standard polynomial space of degree up to k on $[0, 1]$. Therefore, we have $V_n^k = \bigoplus_{0 \leq l \leq n} W_l^k$.

Now we define a set of orthonormal basis associated with the space W_l^k . The case of mesh level $l = 0$ is trivial. We use the normalized shifted Legendre polynomials in $[0, 1]$ and denote the basis by $v_{i,0}^0(x)$ for $i = 1, \dots, k+1$. When $l > 0$, the orthonormal bases in W_l^k are presented in [3] and denoted by

$$v_{i,l}^j(x), \quad i = 1, \dots, k+1, \quad j = 0, \dots, 2^{l-1} - 1.$$

The construction follows a repeated Gram-Schmidt process and the explicit expression of the multiwavelet basis functions are provided in Table 1 in [3]. Note that such multiwavelet bases retain the orthonormal property of wavelet bases for different mesh levels, i.e.,

$$\int_0^1 v_{i,l}^j(x) v_{i',l'}^{j'}(x) dx = \delta_{ii'} \delta_{jj'}. \quad (3)$$

and the support of $v_{i,l}^j$ is in I_{l-1}^j .

Multidimensional case when $d > 1$ follows from a tensor-product approach. First we recall some basic notations. For a multi-index $\alpha = (\alpha_1, \dots, \alpha_d) \in \mathbb{N}_0^d$, where \mathbb{N}_0 denotes the set of nonnegative integers, the l^1 and l^∞ norms are defined as

$$|\alpha|_1 := \sum_{m=1}^d \alpha_m, \quad |\alpha|_\infty := \max_{1 \leq m \leq d} \alpha_m.$$

The component-wise arithmetic operations and relational operations are defined as

$$\alpha \cdot \beta := (\alpha_1 \beta_1, \dots, \alpha_d \beta_d), \quad c \cdot \alpha := (c \alpha_1, \dots, c \alpha_d), \quad 2^\alpha := (2^{\alpha_1}, \dots, 2^{\alpha_d}),$$

$$\alpha \leq \beta \Leftrightarrow \alpha_m \leq \beta_m, \forall m, \quad \alpha < \beta \Leftrightarrow \alpha \leq \beta \text{ and } \alpha \neq \beta.$$

By making use of the multi-index notation, we denote by $\mathbf{l} = (l_1, \dots, l_d) \in \mathbb{N}_0^d$ the mesh level in a multivariate sense. We define the tensor-product mesh grid $\Omega_{\mathbf{l}} = \Omega_{l_1} \otimes \dots \otimes \Omega_{l_d}$ and the corresponding mesh size $h_{\mathbf{l}} = (h_{l_1}, \dots, h_{l_d})$. Based on the grid $\Omega_{\mathbf{l}}$, we denote $I_{\mathbf{l}}^{\mathbf{j}} = \{\mathbf{x} : x_m \in (h_m j_m, h_m(j_m + 1)), m = 1, \dots, d\}$ as an elementary cell, and

$$\mathbf{V}_{\mathbf{l}}^k := \{\mathbf{v} : \mathbf{v}(\mathbf{x}) \in Q^k(I_{\mathbf{l}}^{\mathbf{j}}), \mathbf{0} \leq \mathbf{j} \leq 2^{\mathbf{l}} - \mathbf{1}\} = V_{l_1, x_1}^k \times \dots \times V_{l_d, x_d}^k$$

as the tensor-product piecewise polynomial space, where $Q^k(I_{\mathbf{l}}^{\mathbf{j}})$ represents the collection of polynomials of degree up to k in each dimension on cell $I_{\mathbf{l}}^{\mathbf{j}}$. If we use equal mesh refinement of size $h_N = 2^{-N}$ in each coordinate direction, the grid and space will be denoted by Ω_N and \mathbf{V}_N^k , respectively.

Based on a tensor-product construction, the multidimensional increment space can be defined as

$$\mathbf{W}_{\mathbf{l}}^k = W_{l_1, x_1}^k \times \dots \times W_{l_d, x_d}^k.$$

Therefore, the standard tensor-product piecewise polynomial space on Ω_N can be written as

$$\mathbf{V}_N^k = \bigoplus_{\substack{|\mathbf{l}|_\infty \leq N \\ \mathbf{l} \in \mathbb{N}_0^d}} \mathbf{W}_{\mathbf{l}}^k, \quad (4)$$

while the sparse grid approximation space in [51] is

$$\hat{\mathbf{V}}_N^k := \bigoplus_{\substack{|\mathbf{l}|_1 \leq N \\ \mathbf{l} \in \mathbb{N}_0^d}} \mathbf{W}_{\mathbf{l}}^k \subset \mathbf{V}_N^k. \quad (5)$$

The dimension of $\hat{\mathbf{V}}_N^k$ scales as $O((k+1)^d 2^N N^{d-1})$ [51], which is significantly less than that of \mathbf{V}_N^k with exponential dependence on Nd . The approximation results for $\hat{\mathbf{V}}_N^k$ are discussed in [51, 25], which has a stronger smoothness requirement than the traditional \mathbf{V}_N^k space. In this paper, we will not require the numerical solution to be in $\hat{\mathbf{V}}_N^k$, but rather in \mathbf{V}_N^k and to be chosen adaptively similar to [26].

Finally, we define the basis functions in multidimensions as

$$v_{\mathbf{i},\mathbf{l}}^{\mathbf{j}}(\mathbf{x}) := \prod_{m=1}^d v_{i_m, l_m}^{j_m}(x_m), \quad (6)$$

for $\mathbf{l} \in \mathbb{N}_0^d$, $\mathbf{j} \in B_{\mathbf{l}} := \{\mathbf{j} \in \mathbb{N}_0^d : \mathbf{0} \leq \mathbf{j} \leq \max(2^{\mathbf{l}-1} - \mathbf{1}, \mathbf{0})\}$ and $\mathbf{1} \leq \mathbf{i} \leq \mathbf{k} + \mathbf{1}$. The orthonormality of the bases can be established by (3).

2.2 Interpolatory multiwavelets

Alpert's multiwavelets and the space W_l^k are constructed so that they correspond to the difference of the L^2 projection on adjacent levels. The idea of the sparse grid collocation basis proposed in [49] is to switch the operator to be interpolation on nested grids. Below, we will outline the construction. Denote the set of interpolation points in the interval $I = [0, 1]$ at mesh level 0 by $X_0 = \{x_i\}_{i=0}^P \subset I$. Here, the number of points in X_0 is $(P+1)$. Then the interpolation points at mesh level $n \geq 1$, X_n can be obtained correspondingly as

$$X_n = \{x_{i,n}^j := 2^{-n}(x_i + j), \quad i = 0, \dots, P, \quad j = 0, \dots, 2^n - 1\}.$$

We require the points to be nested, i.e.

$$X_0 \subset X_1 \subset X_2 \subset X_3 \subset \dots. \quad (7)$$

to save computational cost. This can be achieved by requiring $X_0 \subset X_1$, and then one can deduce (7) easily.

Given the nodes, we define the basis functions on the 0-th level grid as Lagrange ($K = 0$) or Hermite ($K \geq 1$) interpolation polynomials of degree $M = (P+1)(K+1) - 1$ which satisfy the property:

$$\phi_{i,l}^{(l')}(x_{i'}) = \delta_{ii'} \delta_{ll'},$$

for $i, i' = 0, \dots, P$ and $l, l' = 0, \dots, K$. It is easy to see that $\text{span}\{\phi_{i,l}, \quad i = 0, \dots, P, \quad l = 0, \dots, K\} = V_0^M$. The constants P, K, M will be specified

later on in the paper. With the basis function at mesh level 0, we can define basis function at mesh level $n \geq 1$:

$$\phi_{i,l,n}^j := 2^{-nl} \phi_{i,l}(2^n x - j), \quad i = 0, \dots, P, \quad l = 0, \dots, K, \quad j = 0, \dots, 2^n - 1$$

which is a complete basis set for V_n^M .

Next, we introduce the hierarchical representations. Define $\tilde{X}_0 := X_0$ and $\tilde{X}_n := X_n/X_{n-1}$ for $n \geq 1$, then we have the decomposition

$$X_n = \tilde{X}_0 \cup \tilde{X}_1 \cup \dots \cup \tilde{X}_n.$$

Denote the points in \tilde{X}_1 by $\tilde{X}_1 = \{\tilde{x}_i\}_{i=0}^P$. Then the points in \tilde{X}_n for $n \geq 1$ can be represented by

$$\tilde{X}_n = \{\tilde{x}_{i,n}^j := 2^{-(n-1)}(\tilde{x}_i + j), \quad i = 0, \dots, P, \quad j = 0, \dots, 2^{n-1} - 1\}.$$

For notational convenience, we let $\tilde{W}_0^M := V_0^M$. The increment function space \tilde{W}_n^M for $n \geq 1$ is introduced as a function space that satisfies

$$V_n^M = V_{n-1}^M \oplus \tilde{W}_n^M, \quad (8)$$

and is defined through the multiwavelets $\psi_{i,l}^{(l')} \in V_1^M$ that satisfies

$$\psi_{i,l}^{(l')}(x_{i'}) = 0, \quad \psi_{i,l}^{(l')}(\tilde{x}_{i'}) = \delta_{i,i'} \delta_{l,l'},$$

for $i, i' = 0, \dots, P$ and $l, l' = 0, \dots, K$. Then W_n^M is given by

$$\tilde{W}_n^M = \text{span}\{\psi_{i,l,n}^j, \quad i = 0, \dots, P, \quad l = 0, \dots, K, \quad j = 0, \dots, 2^{n-1} - 1\}$$

where $\psi_{i,l,n}^j(x) := 2^{-(n-1)l} \psi_{i,l}(2^{n-1}x - j)$. For completeness, we list the basis functions used in this paper in the appendix.

The construction above has close connection with interpolation operators. For a given function $f(x) \in C^{K+1}(I)$, we define $\mathcal{I}_N^{P,K}[f]$ as the standard Hermite interpolation on V_N^M , and have the representation

$$\mathcal{I}_N^{P,K}[f](x) = \sum_{n=0}^N \sum_{j=0}^{\max(2^{n-1}-1, 0)} \sum_{l=0}^K \sum_{i=0}^P b_{i,l,n}^j \psi_{i,l,n}^j(x).$$

Clearly, $(\mathcal{I}_n^{P,K} - \mathcal{I}_{n-1}^{P,K})[f](x) \in \tilde{W}_n^M$. The algorithm converting between the point values and the derivatives $\{f^{(l)}(x_{i,n}^j)\}$ to hierarchical coefficients $\{b_{i,l,n}^j\}$

is given in [49], and by a standard argument in fast wavelet transform, can be performed in $O(M2^n)$ flops.

The multidimensional construction follows similar lines as in Section 2.1. We let

$$\tilde{\mathbf{W}}_1^M = \tilde{W}_{l_1, x_1}^M \times \cdots \times \tilde{W}_{l_d, x_d}^M,$$

Therefore,

$$\mathbf{V}_N^M = \bigoplus_{\substack{|\mathbf{l}|_\infty \leq N \\ \mathbf{l} \in \mathbb{N}_0^d}} \tilde{\mathbf{W}}_1^M,$$

while the sparse grid approximation space is

$$\hat{\mathbf{V}}_N^M = \bigoplus_{\substack{|\mathbf{l}|_1 \leq N \\ \mathbf{l} \in \mathbb{N}_0^d}} \tilde{\mathbf{W}}_1^M.$$

Note that the construction by Alpert's multiwavelet and the interpolatory multiwavelet gives the same sparse grid space. Finally, the interpolation operator in multidimension $\mathcal{I}_N^{P,K} : C^{K+1}(\Omega) \rightarrow \mathbf{V}_N^M$:

$$\mathcal{I}_N^{P,K}[f](\mathbf{x}) = \sum_{\substack{|\mathbf{n}|_\infty \leq N \\ \mathbf{0} \leq \mathbf{j} \leq \max(2^{\mathbf{n}-1} - \mathbf{1}, \mathbf{0}) \\ \mathbf{0} \leq \mathbf{l} \leq \mathbf{K} \\ \mathbf{0} \leq \mathbf{i} \leq \mathbf{P}}} b_{\mathbf{i}, \mathbf{l}, \mathbf{n}}^{\mathbf{j}} \psi_{\mathbf{i}, \mathbf{l}, \mathbf{n}}^{\mathbf{j}}(\mathbf{x}),$$

where the multidimensional basis functions $\psi_{\mathbf{i}, \mathbf{l}, \mathbf{n}}^{\mathbf{j}}(\mathbf{x})$ are defined in the same approach as (6) by tensor products. If the space is switched from \mathbf{V}_N^M to some subset of \mathbf{V}_N^M , e.g. the sparse grid space $\hat{\mathbf{V}}_N^M$ or some other subset of \mathbf{V}_N^M that is dynamically chosen, the interpolation operator can be defined accordingly, taking only multiwavelet basis functions that belong to that space.

3 Adaptive multiresolution DG evolution algorithm

In this section, we will describe the adaptive multiresolution DG scheme for (1). We will first introduce the DG scheme with multiresolution interpolation. The accuracy requirement for the interpolation operator is studied by local truncation error analysis. We then describe the adaptive strategy. Finally, the artificial viscosity is introduced based on the estimate of the coefficients of the hierarchical basis functions.

3.1 DG scheme with multiresolution interpolation

First, we review some basis notations about meshes. Let N be the maximum mesh level and T_h be the collection of all elementary cell T_N^j , $0 \leq j_m \leq 2^N - 1$, $\forall m = 1, \dots, d$. Define $\Gamma_h := \bigcup_{K \in T_h} \partial K$ be the union of all the interfaces for all the elements in T_h . Here, for simplicity, we formulate the scheme with periodic boundary conditions, while we keep in mind other boundary conditions can be treated in the DG framework as well.

The semi-discrete DG scheme for the scalar conservation law reads as [15]

$$\sum_{K \in T_h} \int_K (u_h)_t v_h dx - \sum_{K \in T_h} \int_K f(u_h) \cdot \nabla v_h dx + \sum_{e \in \Gamma_h} \int_e \widehat{f \cdot n_K}(u_h) v_h ds = 0. \quad (9)$$

Here, u_h is the numerical solution and v_h is the test function. The numerical flux $\widehat{f \cdot n_K}(u_h) \equiv \widehat{f \cdot n_K}(u_h^{int}, u_h^{ext})$ is taken to be the global Lax-Friedrichs flux:

$$\widehat{f \cdot n_K}(a, b) = \frac{1}{2} (f(a) + f(b)) \cdot n_K - \frac{1}{2} C(b - a), \quad (10)$$

where $C = \max_u |n_K \cdot f'(u)|$ and the maximum is taken over the whole domain. u_h, v_h belong to the same function space \mathbf{V}^k . If $\mathbf{V}^k = \mathbf{V}_N^k$, we recover the standard (or full grid) DG method. If $\mathbf{V}^k = \hat{\mathbf{V}}_N^k$, we obtain the sparse grid DG method. In this paper, we will take \mathbf{V}^k as a subset of \mathbf{V}_N^k that is chosen adaptively as outlined in Section 3.2.

In DG methods, the integrals over elements and edges are often approximated by numerical quadrature rules on each cell [13]. However, in sparse grid DG method, this naive approach would result in computational cost that is proportional to the number of fundamental elements, i.e., $\mathcal{O}(h^{-d})$, and is still subject to the curse of dimensionality. To evaluate the integrals over elements and edges more efficiently with a cost proportional to the DoF of the underlying finite element space, we interpolate the nonlinear function $f(u_h)$ by using the multiresolution Lagrange (or Hermite) interpolation basis functions introduced in Section 2.2. Therefore, the semi-discrete DG scheme with interpolation is

$$\sum_{K \in T_h} \int_K (u_h)_t v_h dx - \sum_{K \in T_h} \int_K \mathcal{I}[f(u_h)] \cdot \nabla v_h dx + \sum_{e \in \Gamma_h} \int_e \mathcal{I}[\widehat{f \cdot n_K}(u_h)] v_h ds = 0, \quad (11)$$

where $\mathcal{I}[\cdot]$ is a multiresolution interpolation operator onto some finite element space with the same multiresolution structure as \mathbf{V}^k , but of polynomial degree M . The choice of $\mathcal{I}[\cdot]$ will be specified later, which plays important roles

in numerical stability and accuracy. Note that the numerical flux $\widehat{f \cdot n_K}(u_h)$ is only defined at edges, thus it remains to clarify the meaning of the interpolation $\mathcal{I}[\widehat{f \cdot n_K}(u_h)]$. Since we use the global Lax-Friedrichs flux (10), we have

$$\begin{aligned}\mathcal{I}[\widehat{f \cdot n_K}(u_h^{int}, u_h^{ext})] &= \frac{1}{2} (\mathcal{I}[f(u_h^{int})] + \mathcal{I}[f(u_h^{ext})]) \cdot n_K - \frac{1}{2} C(\mathcal{I}[u_h^{ext}] - \mathcal{I}[u_h^{int}]) \\ &= \frac{1}{2} (\mathcal{I}[f(u_h^{int})] + \mathcal{I}[f(u_h^{ext})]) \cdot n_K - \frac{1}{2} C(u_h^{ext} - u_h^{int})\end{aligned}$$

due to the linearity of the interpolation operator $\mathcal{I}[\cdot]$. Therefore, we only need to obtain the interpolation $\mathcal{I}[f(u_h)]$ and then read the value on two sides of the edges to obtain $\mathcal{I}[f(u_h^{int})]$ and $\mathcal{I}[f(u_h^{ext})]$. Now, we discuss about numerical implementation. First, we read the (derivative) values of u_h , which is a linear combination of Alpert's basis functions at the chosen interpolation points. Second, we calculate the (derivative) values of $f(u_h)$ at these interpolation points. Last, we transfer the (derivative) values to coefficients of interpolation basis, by using the algorithm introduced in [49]. At this point, the numerical integrations can be performed through a fast matrix-vector product as in [46]. We remark that the computational cost does not increase too much compared to the multiresolution DG schemes for linear equations introduced in [26]. The cost of the transformation from the (derivative) values to hierarchical coefficients is only *linearly* dependent on the dimension d [49].

Now we discuss the choice of $\mathcal{I}[\cdot]$. To preserve the accuracy of the original DG scheme (9), it is required that the interpolation operator $\mathcal{I}[\cdot]$ reaches certain accuracy. Following [13], we rewrite the weak formulation (11) in the ODE form as

$$\frac{du_h}{dt} = L_h(u_h), \quad (12)$$

where $L_h(u)$ is an operator onto \mathbf{V}^k , which is a discrete approximation of $-\nabla \cdot f(u)$ and satisfies

$$\sum_{K \in \mathcal{T}_h} \int_K L_h(u_h) v_h dx = \sum_{K \in \mathcal{T}_h} \int_K \mathcal{I}[f(u_h)] \cdot \nabla v_h dx - \sum_{e \in \Gamma_h} \int_e \mathcal{I}[\widehat{f \cdot n_K}(u_h)] v_h ds. \quad (13)$$

To illustrate the ideas, we only consider the full grid or sparse grid DG methods, i.e. $\mathbf{V}^k = \mathbf{V}_N^k$ or $\mathbf{V}^k = \hat{\mathbf{V}}_N^k$. For adaptive methods, similar intuitive arguments can be made, but rigorous proof is much harder. Using similar

error estimates techniques in [13, 34], we have the following proposition on local truncation error:

Proposition 3.1 (Accuracy of semi-discrete DG scheme with interpolation). *Assume that the DG finite element space (standard or sparse) has polynomials up to degree k , if the interpolation operator in (11) has the accuracy of h^{k+2} (standard) or $|\log_2 h|^d h^{k+2}$ (sparse) for sufficiently smooth functions, then the truncation error of the semi-discrete DG scheme with interpolation (11) is of order h^{k+1} (standard) or $|\log_2 h|^d h^{k+1}$ (sparse). To be more precise, for sufficiently smooth function u , the standard DG with interpolation (11) has the truncation error:*

$$\|L_h(u) + \nabla \cdot f(u)\|_{L^2(\Omega)} \leq Ch^{k+1}, \quad (14)$$

and the sparse grid DG with interpolation (11) has the truncation error:

$$\|L_h(u) + \nabla \cdot f(u)\|_{L^2(\Omega)} \leq C |\log_2 h|^d h^{k+1}. \quad (15)$$

Here, the constant C may depend on the solution, but does not depend on h .

Proof. To save space, we only show the proof for full grid DG space $\mathbf{V}^k = \mathbf{V}_N^k$. Similar technique also applies to the sparse grid DG space using projection error estimates in [25].

We denote the standard L^2 projection operator onto the standard DG finite element space by \mathbb{P} , then

$$\|L_h(u) + \nabla \cdot f(u)\|_{L^2(\Omega)} \leq e_1 + e_2, \quad (16)$$

where

$$e_1 := \|L_h(u) + \mathbb{P}(\nabla \cdot f(u))\|_{L^2(\Omega)},$$

and

$$e_2 := \|\mathbb{P}(\nabla \cdot f(u)) - \nabla \cdot f(u)\|_{L^2(\Omega)}.$$

The estimate for e_2 is trivial using projection properties:

$$e_2 \leq Ch^{k+1} \|\nabla \cdot f(u)\|_{H^{k+1}(\Omega)}. \quad (17)$$

To estimate e_1 , we consider any test function v_h in DG space, and obtain

$$\sum_{K \in T_h} \int_K (L_h(u) + \mathbb{P}(\nabla \cdot f(u))) v_h = \sum_{K \in T_h} \int_K (L_h(u) + \nabla \cdot f(u)) v_h$$

$$\begin{aligned}
&= \sum_{K \in T_h} \int_K \mathcal{I}[f(u)] \cdot \nabla v_h - \sum_{e \in \Gamma_h} \int_e \mathcal{I}[\widehat{f \cdot n_K}(u)] \cdot n_K v_h ds \\
&\quad - \sum_{K \in T_h} \int_K (f(u) \cdot \nabla v_h) + \sum_{e \in \Gamma_h} \int_e f(u) \cdot n_K v_h ds \\
&= \sum_{K \in T_h} \int_K (\mathcal{I}[f(u)] - f(u)) \cdot \nabla v_h - \sum_{e \in \Gamma_h} \int_e (\mathcal{I}[f(u) \cdot n_K] - f(u) \cdot n_K) v_h ds \\
&\leq \|\mathcal{I}[f(u)] - f(u)\|_{L^2(\Omega)} \|\nabla v_h\|_{L^2(\Omega)} + \|\mathcal{I}[f(u)] - f(u)\|_{L^2(\Gamma_h)} \|v_h\|_{L^2(\Gamma_h)} \\
&\leq Ch^{k+2} h^{-1} \|v_h\|_{L^2(\Omega)} + Ch^{-\frac{1}{2}} h^{k+2} h^{-\frac{1}{2}} \|v_h\|_{L^2(\Omega)} \\
&= Ch^{k+1} \|v_h\|_{L^2(\Omega)}.
\end{aligned}$$

Here we use the multiplicative trace inequality and the inverse inequality, see e.g. Lemma 2.1 and Lemma 2.3 in [34]. We take v_h to be $(L_h(u) + \mathbb{P}(\nabla \cdot f(u)))$ in the inequality above and have

$$\|L_h(u) + \mathbb{P}(\nabla \cdot f(u))\|_{L^2(\Omega)}^2 \leq Ch^{k+1} \|L_h(u) + \mathbb{P}(\nabla \cdot f(u))\|_{L^2(\Omega)}$$

and eventually arrive at

$$e_1 = \|L_h(u) + \mathbb{P}(\nabla \cdot f(u))\|_{L^2(\Omega)} \leq Ch^{k+1}. \quad (18)$$

Combining (18) and (17), we have the estimate for the truncation error (14). \square

From the proposition above, we find that, one has to apply the interpolation in which the function space has polynomials of one degree higher than the original DG function space, if one would like to preserve the order of accuracy for the original (standard or sparse grid) DG scheme, i.e. we shall require $M \geq k + 1$. For example, if we take quadratic polynomials for the DG space, then it is required to apply P^3 interpolation operator (Lagrange or Hermite interpolation) to treat the nonlinear terms. From our numerical test, it seems that it is not a necessary condition for the standard DG method, but it is necessary for the sparse grid DG method.

In Proposition 3.1, we only estimate the truncation error, and this is far from rigorous error estimate that takes into account stability. In numerical experiments, we observe that the standard DG is stable with the Lagrange interpolation. However, the sparse grid DG with Lagrange interpolation is *weakly* unstable and will blow up with very fine mesh for polynomials of

high degrees (see the numerical results in Table 2 and Table 3 in Section 4). With Hermite interpolation, the sparse grid DG scheme is more stable and produce satisfactory convergence rate (see Table 4 in Section 4). Actually, for standard DG with quadrature rules applied in each element, if the truncation error satisfies the required order of accuracy, then the convergence and error estimate can be guaranteed [34]. However, it is not true for the sparse grid DG method from our numerical experiments. This indicates that the standard DG method is more stable than the sparse grid DG method in this sense. We also remark that, since the interpolation operator introduced here is global but not local, the approach in [34] would probably fail to obtain the rigorous error estimate here. We will leave the detailed analysis as future work.

3.2 Adaptivity

In this section, we review the adaptive procedure introduced in [26] to determine the space \mathbf{V}^k . The method is very similar to those in [26], except that two sets of basis functions are involved and they are adaptively chosen at the same time.

In the adaptive DG algorithm, we specify the maximum mesh level N and an accuracy threshold $\epsilon > 0$. Details on the optimal choice of ϵ can be found for example in [33]. The same adaptive multiresolution projection method in [26] is applied here as the numerical initial condition for DG schemes. The error indicator using L^2 norm is used. The details are omitted and we refer readers to Algorithm 1 in [26].

The scheme is implemented by hash table as the underlying data structure. We now introduce the concepts of child, parent and leaf elements. If an element $V_{\mathbf{l}'}^{\mathbf{j}'}$ with $|\mathbf{l}'|_\infty \leq N$ satisfies the condition that there exists an integer m such that $1 \leq m \leq d$ and $\mathbf{l}' = \mathbf{l} + \mathbf{e}_m$, where \mathbf{e}_m denotes the unit vector in the x_m direction, and the support of $V_{\mathbf{l}'}^{\mathbf{j}'}$ is within that of $V_{\mathbf{l}}^{\mathbf{j}}$, then $V_{\mathbf{l}'}^{\mathbf{j}'}$ is called a child element of $V_{\mathbf{l}}^{\mathbf{j}}$. Accordingly, element $V_{\mathbf{l}}^{\mathbf{j}}$ is called a parent element of $V_{\mathbf{l}'}^{\mathbf{j}'}$. If an element does not have its child element in the hash table, then we call it a leaf element.

The time evolution consists of four steps. The first step is the prediction step, which means given the hash table H that stores the numerical solution u_h at time step t^n and the associated leaf table L , we need to predict the location where the details becomes significant at the next time step t^{n+1} ,

then add more elements in order to capture the fine structures. We solve for $u_h \in \mathbf{V}_{N,H}^k$ from t^n to t^{n+1} using a cheap solver, e.g. the forward Euler discretization. Here, the interpolation operator $\mathcal{I}[\cdot]$ is determined by accuracy requirement, and has the same multiresolution structure as determined by the hash table H corresponding to the numerical solution u_h . The predicted solution at t^{n+1} is denoted by $u_h^{(p)}$. Note that to save cost, that the artificial viscosity term as introduced in Section 3.3 does not need to be included in the prediction step.

The second step is the refinement step according to the predicted solution $u_h^{(p)}$. We traverse the hash table H and if an element V_1^j satisfies the refinement criteria

$$\left(\sum_{1 \leq i \leq k+1} |w_{i,1}^j|^2 \right)^{1/2} \geq \epsilon, \quad (19)$$

where $w_{i,1}^j$ denotes the hierarchical coefficient corresponding to the basis $v_{i,1}^j(\mathbf{x})$, i.e. $w_{i,1}^j = \int_{\Omega} u(\mathbf{x}) v_{i,1}^j(\mathbf{x}) d\mathbf{x}$. (19) indicates that such an element becomes significant at the next time step, then we need to refine the mesh by adding its children elements to H . The detailed procedure is described as follows. For a child element $V_{l'}^{j'}$ of V_1^j , if it has been already added to H , i.e. $V_{l'}^{j'} \in H$, we do nothing; if not, we add the element $V_{l'}^{j'}$ to H and let the associated detail coefficients $w_{i,l'}^{j'} = 0$, $1 \leq i \leq k+1$. Moreover, we need to increase the number of children by one for all elements that has $V_{l'}^{j'}$ as its child element and remove the parent elements of $V_{l'}^{j'}$ from the leaf table if they have been added. Finally, we obtain a larger hash table $H^{(p)}$ and the associated approximation space $\mathbf{V}_{N,H^{(p)}}^k$ and the leaf table $L^{(p)}$.

Then, based on the updated hash table $H^{(p)}$, we evolve the numerical solution by the DG formulation with space $\mathbf{V}_{N,H^{(p)}}^k$. Namely, we solve for $\mathbf{V}_{N,H^{(p)}}^k$ from t^n to t^{n+1} , to generate the precoarsened solution \tilde{u}_h^{n+1} , by using the the accurate solver with artificial viscosity in Section 3.3. Here, the interpolation operator should determined by the updated hash table $H^{(p)}$. Note that in the artificial viscosity $\nu = \nu(u_h)$ we fix u_h to be u_h^n such that the matrix for the diffusion term only need to be resembled one time in each time step.

The last step is to coarsen by removing elements that become insignificant at time level t^{n+1} . The hash table $H^{(p)}$ that stores the numerical solution \tilde{u}_h^{n+1} is recursively coarsened by the following procedure. The leaf table $L^{(p)}$

is traversed, and if an element $V_1^j \in L^{(p)}$ satisfies the coarsening criterion

$$\left(\sum_{1 \leq i \leq k+1} |w_{i,1}^j|^2 \right)^{\frac{1}{2}} < \eta, \quad (20)$$

where η is a prescribed error constant, then we remove the element from both table $L^{(p)}$ and $H^{(p)}$, and set the associated coefficients $w_{i,1'}^j = 0$, $1 \leq i \leq k+1$. For each of its parent elements in table $H^{(p)}$, we decrease the number of children by one. If the number becomes zero, i.e, the element has no child any more, then it is added to the leaf table $L^{(p)}$ accordingly. Repeat the coarsening procedure until no element can be removed from the table $L^{(p)}$. By removing only the leaf element at each time, we avoid generating “holes” in the hash table. The output of this coarsening procedure are the updated hash table and leaf table, denoted by H and L respectively, and the compressed numerical solution $u_h^{n+1} \in \mathbf{V}_{N,H}^k$. In practice, η is chosen to be smaller than ε for safety. In the simulations presented in this paper, we use $\eta = \varepsilon/10$.

3.3 Artificial viscosity

For capturing shock, we add artificial viscosity following the approach in [6] and arrive at the semi-discrete formulation

$$\begin{aligned} \sum_{K \in T_h} \int_K (u_h)_t v_h d\mathbf{x} - \sum_{K \in T_h} \int_K \mathcal{I}[f(u_h)] \cdot \nabla v_h d\mathbf{x} + \sum_{e \in \Gamma_h} \int_e \mathcal{I}[\widehat{f \cdot n_K}(u_h)] v_h ds \\ - \sum_{K \in T_h} \int_K \nu(u_h) \nabla u_h \cdot \nabla v_h d\mathbf{x} = 0. \end{aligned} \quad (21)$$

where $\nu = \nu(u_h) \geq 0$ is the artificial viscosity. The artificial viscosity is piecewise constant in each element and depends on u_h . It is only imposed in the leaf element (since the sharp gradient and shock will only appear in the leaf element) and is determined in the following approach:

$$\nu = \begin{cases} 0, & \text{if } s_e \leq s_0 + \kappa, \\ \nu_0 h, & \text{otherwise.} \end{cases}$$

where $\nu_0 > 0$ and κ are constants chosen empirically. In the numerical experiments, we typically take $\nu_0 = 1$ and $\kappa = 0$. The parameters s_e and s_0

are given as

$$s_e = \log_{10} \left(\sum_{1 \leq \mathbf{i} \leq \mathbf{k}+1} |w_{\mathbf{i},\mathbf{l}}^{\mathbf{j}}|^2 \right)^{\frac{1}{2}}, \quad s_0 = \log_{10} (2^{-(k+\frac{1}{2})|\mathbf{l}|_1}). \quad (22)$$

In the regions where the solutions are smooth, s_e should be the same order as s_0 . If the solution is discontinuous, s_e should be much larger than s_0 .

This smoothness indicator is motivated by the estimate of the coefficients of hierarchical basis functions in [25, 26]. It is shown in [25, 26] that for a function $u(\mathbf{x}) \in H^{p+1}(\Omega)$,

$$\left(\sum_{\substack{0 \leq \mathbf{j} \leq \max(2^{\mathbf{l}-1}-1, \mathbf{0}) \\ 1 \leq \mathbf{i} \leq \mathbf{k}+1}} |w_{\mathbf{i},\mathbf{l}}^{\mathbf{j}}|^2 \right)^{1/2} \leq C 2^{-(q+1)|\mathbf{l}|_1} |u|_{H^{p+1}(\Omega)}, \quad (23)$$

where $q = \min\{p, k\}$, and C is a constant independent of mesh level \mathbf{l} . Therefore, by assuming that $u \in W^{p+1,\infty}(\Omega)$, we can obtain a local estimate in each element on mesh level \mathbf{l} : for any index \mathbf{j} ,

$$\left(\sum_{1 \leq \mathbf{i} \leq \mathbf{k}+1} |w_{\mathbf{i},\mathbf{l}}^{\mathbf{j}}|^2 \right)^{1/2} \leq C 2^{-(q+\frac{1}{2})|\mathbf{l}|_1} |u|_{W^{p+1,\infty}(\Omega)}. \quad (24)$$

Therefore, for sufficiently smooth functions, the coefficients should decay like

$$\left(\sum_{1 \leq \mathbf{i} \leq \mathbf{k}+1} |w_{\mathbf{i},\mathbf{l}}^{\mathbf{j}}|^2 \right)^{1/2} \sim 2^{-(k+\frac{1}{2})|\mathbf{l}|_1}. \quad (25)$$

Remark 3.1. *There are still many problems to be explored on the artificial viscosity. The first one is the specific form of the artificial viscosity term. Here, for simplicity, we only add an artificial viscosity term $\int \nu(u_h) \nabla u_h \cdot \nabla v_h$ in (21). One may also add a physical diffusion term $\nabla \cdot (\nabla \nu(u) u)$ and then discrete it using local DG [42] or interior penalty DG [37]. The second issue is how to choose the optimal parameters κ and ν_0 in the artificial viscosity to obtain a sharp shock profile. The artificial neural network introduced in [44, 19] might be helpful for this problem. We will explore these subjects in future work.*

The diffusion coefficient $\nu(u_h)$ is of order $\mathcal{O}(h)$ for trouble cells and zero for normal cells. Thus, the explicit time integration in both convection and diffusion terms in (21) will yield CFL condition $\Delta t = \mathcal{O}(h)$. For hyperbolic problems $u_t = u_x$ with DG discretizations using polynomials of degree k and

upwind numerical flux and a $(k+1)$ stage explicit RK method of order $(k+1)$, the CFL constant is around $\frac{1}{2k+1}$ [16]. However, for solving diffusion equation $u_t = u_{xx}$ with local DG discretization with polynomials and alternating numerical flux, the CFL constant is around 0.0555 for $k = 1$, 0.0169 for $k = 2$, 0.0063 for $k = 3$, and 0.003 for $k = 4$, if coupled with explicit Runge-Kutta methods of the corresponding order¹, which is much smaller than the CFL constant for convection terms, especially for polynomials of high degrees. If the alternating numerical flux is replaced by the central flux for the diffusion equation, the CFL constant is slightly larger but still much smaller than the CFL constant for the convection part: 0.125 for $k = 1$, 0.0384 for $k = 2$, 0.0158 for $k = 3$ and 0.0083 for $k = 4$.

To obtain better computational efficiency, we avoid explicit time integrations and apply the IMEX time discretizations where the convection term is treated explicitly and the diffusion term implicitly. Here, we only present the third-order IMEX method introduced in [41], which will be coupled with the DG space of quadratic polynomials. The explicit part is the same with the explicit third-order strong stability preserving (SSP) Runge-Kutta method [47] and the implicit part has four stages. To be precise, for the ODE systems:

$$\frac{dU}{dt} = F(U) + G(U), \quad (26)$$

where $F(U)$ denotes the non-stiff term (convection parts) and $G(U)$ the stiff term (diffusion parts). The IMEX scheme for (26) reads as

$$U^{(i)} = U^n + \Delta t \sum_{j=1}^{i-1} \tilde{a}_{ij} F(U^{(j)}) + \Delta t \sum_{j=1}^i a_{ij} G(u^{(j)}), \quad i = 1, \dots, \nu, \quad (27a)$$

$$U^{n+1} = U^n + \Delta t \sum_{i=1}^{\nu} \tilde{w}_i F(U^{(i)}) + \Delta t \sum_{i=1}^{\nu} w_i G(u^{(i)}), \quad (27b)$$

with the stage $\nu = 4$ and the parameters

$$\begin{aligned} \tilde{a}_{32} = 1, \tilde{a}_{42} = \tilde{a}_{43} = \frac{1}{4}, a_{11} = a_{22} = a_{33} = a_{44} = \alpha, a_{21} = -\alpha, a_{32} = 1 - \alpha, \\ a_{41} = \beta, a_{42} = \eta, a_{43} = \frac{1}{2} - \beta - \eta - \alpha, \tilde{w}_2 = \tilde{w}_3 = w_2 = w_3 = \frac{1}{6}, \tilde{w}_4 = w_4 = \frac{2}{3}, \end{aligned}$$

¹The CFL constants are provided by Chi-Wang Shu from Brown University in personal communications.

and

$$\alpha = 0.24169426078821, \quad \beta = 0.06042356519705, \quad \eta = 0.12915286960590.$$

The other parameters not listed above are zero.

By using the IMEX time integrator, the time step restriction remains the same as determined by the convection term. Note that the artificial viscosity $\nu = \nu(u)$ is determined by u_h^n and will keep unchanged in the middle stages of time evolution from t^n to t^{n+1} . Therefore, the matrix for the diffusion term only need to be resembled one time in each time step. Also, we only need to solve a linear system in which the coefficient matrix is symmetric positive definite and also sparse (there exist only a small portion of elements with non-zero viscosity). In the computation, we apply the conjugate gradient method to solve this linear system. We also remark that, for smooth solutions, this scheme will reduce to the explicit time integrations when coupled with the semi-discrete DG scheme with artificial viscosity (21), since the artificial viscosity will automatically vanish and then IMEX scheme (27) reduces to the third-order SSP RK method.

4 Numerical results

In this section, we perform numerical experiments to validate the accuracy and robustness of our scheme. The computational domain is $[0, 1]$ for 1D and $[0, 1]^2$ for 2D. Periodic boundary condition is imposed. When testing accuracy for smooth solutions, we apply the TVD Runge-Kutta time discretizations [47]: second-order RK method for the piecewise linear finite element space ($k = 1$) and third-order RK method for the quadratic ($k = 2$) and cubic ($k = 3$) finite element space. When testing the capability for capturing discontinuous solutions, we use the quadratic finite element space ($k = 2$) coupled with the third-order IMEX time discretizations (27).

Example 4.1 (1D linear advection with constant coefficient). *In this example, we consider the 1D linear advection equation with constant coefficient:*

$$u_t + u_x = 0, \tag{28}$$

with the initial value $u(x, 0) = u_0(x)$. Since the equation is linear, the interpolation operator is not needed. We focus on a non-smooth initial condition

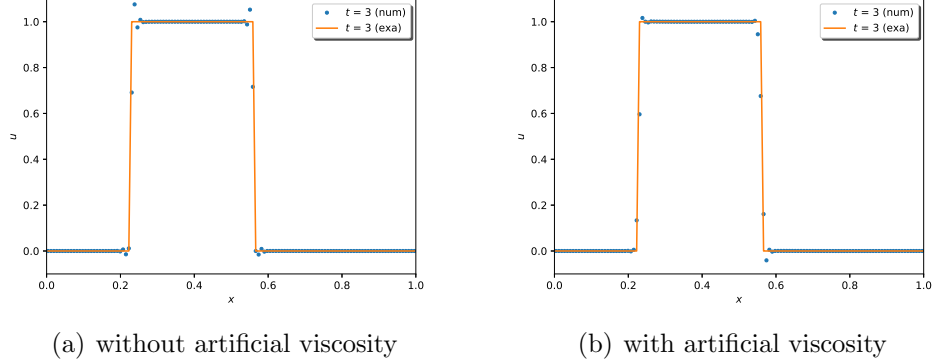


Figure 1: Example 4.1: 1D linear advection with constant coefficient at $t = 3$. Left: without artificial viscosity; right: with artificial viscosity. The solid lines are the exact solution and the symbols are the numerical solutions.

to test the effectiveness of adaptivity and the artificial viscosity. The initial condition is chosen as:

$$u_0(x) = \begin{cases} 1, & 0.23 < x < 0.56, \\ 0, & \text{otherwise.} \end{cases} \quad (29)$$

We set $N = 8$ and $\epsilon = 10^{-5}$. The solutions with and without artificial viscosity at $t = 3$ are presented in Fig. 1. We observe that the multiresolution DG method without artificial viscosity as in [26] can also produce well-resolved solution. With the artificial viscosity, the oscillations are suppressed.

In Fig. 2, the degrees of freedom for scheme with and without artificial viscosity are presented. Since the artificial viscosity (diffusion term) can smoothen the solution, the method has fewer degrees of freedom and thus less computational cost.

Example 4.2 (1D Burgers' equation). In this example, we focus on the 1D Burgers' equation.

$$u_t + (u^2/2)_x = 0,$$

with the initial value $u(x, 0) = u_0(x) = \sin(2\pi x) + \frac{1}{2}$. The shock begins to develop at $t = \frac{1}{2\pi} \approx 0.159$. For this example, we only focus on the non-smooth solution, and defer the accuracy study for smooth solution to the next example in 2D. The adaptive multiresolution DG scheme without artificial viscosity

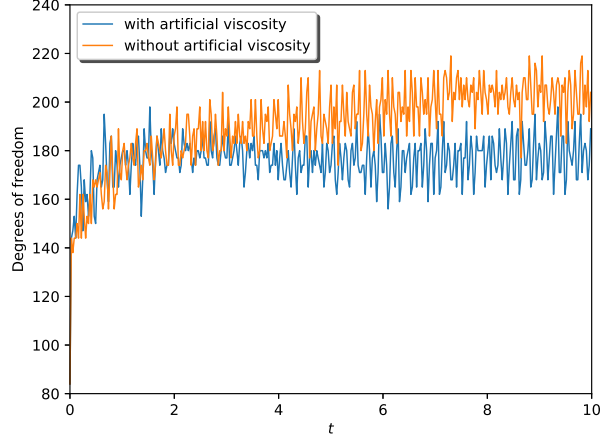


Figure 2: Example 4.1: 1D linear advection with constant coefficient. Time histories of the number of active degrees of freedom with and without artificial viscosity.

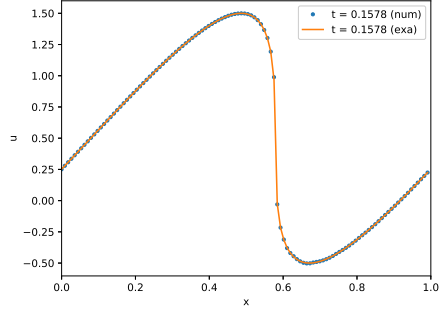
will blow up when the shock develops. We run the code up to time $t = 0.2$, with maximum mesh level is $N = 8$. The solutions obtained with artificial viscosity are shown in Fig. 3 with $\epsilon = 10^{-3}$ and Fig. 4 with $\epsilon = 10^{-4}$. Our scheme can capture the shock very well. We also observe that the leaf elements concentrate near the shock. The artificial viscosity is only imposed on elements near the shock.

Example 4.3 (2D Burgers' equation). In this example, we consider the 2D Burgers' equation:

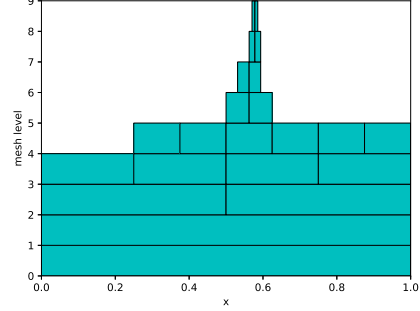
$$u_t + (u^2/2)_x + (u^2/2)_y = 0,$$

with the initial value $u = u_0(x, y) = \sin(2\pi(x + y))$.

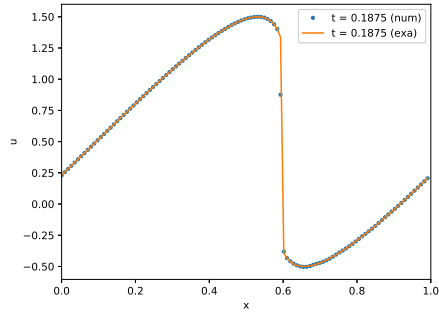
To study the effect of the interpolation operator, we first test the convergence rates for smooth solutions without adaptivity and artificial viscosity. The code is run up to $T = 0.01$. Table 1 shows the convergence rate of the standard DG with integrals over elements and edges calculated by Lagrange interpolation techniques. The interpolation points are imposed in the inner domain, see the interpolation points and basis functions in Appendix A.1. Recall, the degree of polynomials for the DG finite element space is denoted by k and the degree of interpolation operator is denoted by M . It shows almost full



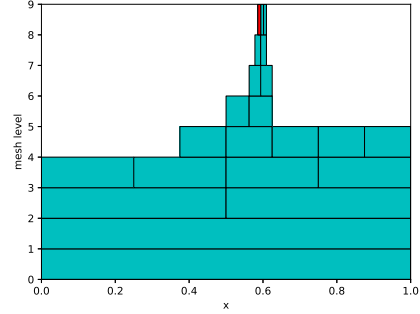
(a) solution profile at $t = 0.1578$



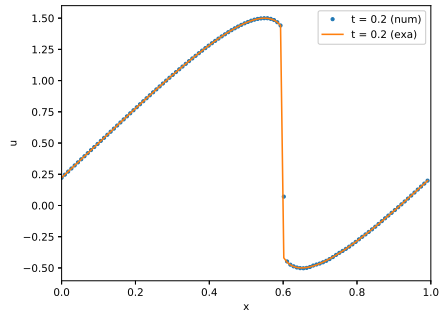
(b) supports of active elements and elements with artificial viscosity $t = 0.1578$



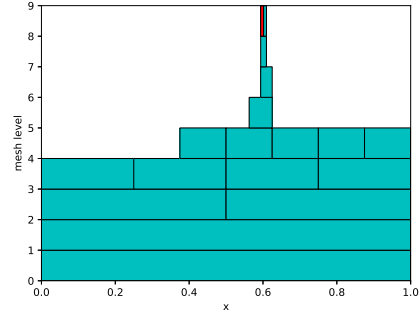
(c) solution profile at $t = 0.1875$



(d) supports of active elements and elements with artificial viscosity at $t = 0.1875$

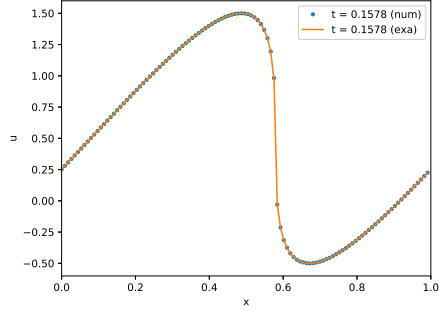


(e) solution profile at $t = 0.2$

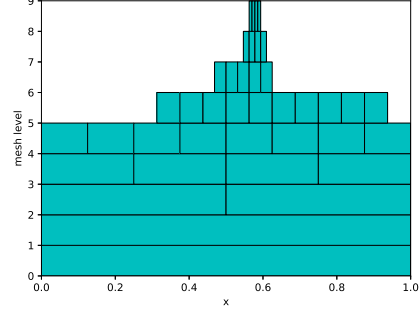


(f) supports of active elements and elements with artificial viscosity at $t = 0.2$

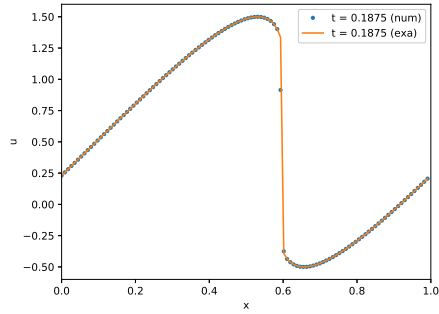
Figure 3: Example 4.2: 1D Burgers' equation at $t = 0.1578, 0.1875$ and 0.2 . $N = 8$ and $\epsilon = 10^{-3}$. Left: solution profile; right: blue color denotes supports of active elements, and red color denotes elements with non-zero artificial viscosity.



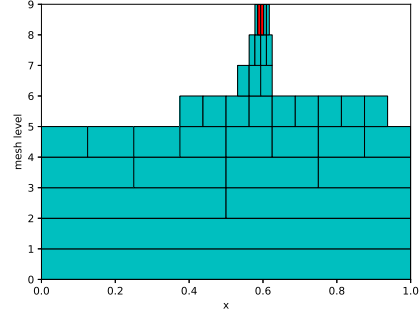
(a) solution profile at $t = 0.1578$



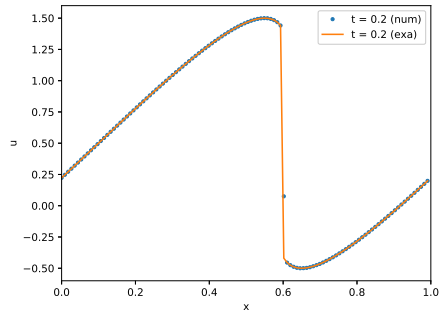
(b) supports of active elements and elements with artificial viscosity $t = 0.1578$



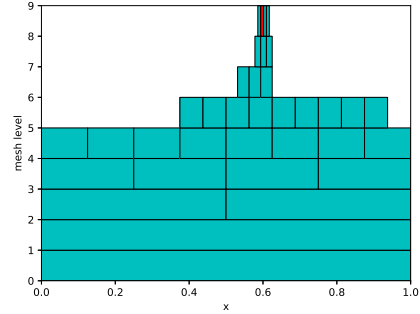
(c) solution profile at $t = 0.1875$



(d) supports of active elements and elements with artificial viscosity at $t = 0.1875$



(e) solution profile at $t = 0.2$



(f) supports of active elements and elements with artificial viscosity at $t = 0.2$

Figure 4: Example 4.2: 1D Burgers' equation at $t = 0.1578, 0.1875$ and 0.2 . $N = 8$ and $\epsilon = 10^{-4}$. Left: solution profile; right: blue color denotes supports of active elements, and red color denotes elements with non-zero artificial viscosity.

convergence rate, except some order reduction when $k = 2$ and $M = 2$, similar to previous results in [34]. Actually, for $k = 2$ and $M = 4$, the numerical scheme is the same as the DG scheme in which the integrals are evaluated exactly, since the physical flux for Burgers' equation is a quadratic function. It seems that the convergence rate is almost full order with $k = 1$ and $M = 1$. Therefore, the condition assumed in Proposition 3.1 may not be necessary for the standard DG method. We also test the accuracy using the Lagrange interpolation in which the interpolation points are at the interface (see the interpolation points and basis functions in Appendix A.2). The results are similar to those in Table 1, and thus they are not presented here for saving space. The Hermite interpolations with $k = 1, M = 3$ and $k = 2, M = 3$ and $k = 3, M = 5$ (see the interpolation points and basis functions in Appendix B) are also tested. The same results are observed and are omitted for brevity.

Next, we test the convergence rate of the sparse grid DG method. We apply three different types of interpolation. The first one is the Lagrange interpolation with the interpolation points at the inner points of elements. The results are shown in Table 2, some weak instability is observed for very fine mesh with $k = 2$. The second one is the the Lagrange interpolation with the interpolation points at the interface. The results are shown in Table 3. The results are better than the first type. For $k = 1$ and $M = 2$, the convergence order is around 1.5, as predicted. For $k = 2$, the convergence order is around 2 with $M = 2$. This indicate that the condition in Proposition 3.1 is necessary here. For $k = 2$ and $M = 3$, there still exists some weak instability for very fine mesh. This motivates us to apply the Hermite interpolation in which we only use the end points. As shown in Table 4, the scheme with the Hermite interpolation is stable with predicted accuracy. This numerical experiment reveals that the Hermite interpolation is more stable than the Lagrange interpolation, and should be the method of choice.

Next, we discuss the convergence rate with adaptivity. Following [26], two types rates of convergence are calculated. The first one is the convergence rate with respect to the error threshold:

$$R_{\epsilon_l} = \frac{\log(e_{l-1}/e_l)}{\log(\epsilon_{l-1}/\epsilon_l)}.$$

The second one is the convergence rate with respect to degrees of freedom:

$$R_{DoF_l} = \frac{\log(e_{l-1}/e_l)}{\log(DoF_{l-1}/DoF_l)}.$$

Table 1: 2D Burgers' equation at $T = 0.01$, $\Delta t = 0.1h$, standard DG, Lagrange interpolation with inner interpolation points.

poly degrees	N	L ¹ -error	order	L ² -error	order	L [∞] -error	order
$k = 1,$ $M = 1$	2	6.58e-02	-	9.31e-02	-	1.94e-01	-
	3	1.88e-02	1.81	2.51e-02	1.89	6.51e-02	1.58
	4	5.74e-03	1.71	7.12e-03	1.82	2.09e-02	1.64
	5	1.69e-03	1.76	2.04e-03	1.80	6.34e-03	1.72
$k = 1,$ $M = 2$	2	6.73e-02	-	9.37e-02	-	1.98e-01	-
	3	1.80e-02	1.90	2.52e-02	1.90	7.11e-02	1.47
	4	5.09e-03	1.82	6.93e-03	1.86	2.16e-02	1.72
	5	1.47e-03	1.79	1.93e-03	1.84	6.55e-03	1.72
$k = 2,$ $M = 2$	2	9.78e-03	-	1.59e-02	-	5.50e-02	-
	3	2.14e-03	2.19	2.67e-03	2.58	1.00e-02	2.46
	4	5.14e-04	2.06	6.69e-04	2.00	2.79e-03	1.84
	5	1.09e-04	2.24	1.45e-04	2.21	5.51e-04	2.34
$k = 2,$ $M = 3$	2	3.55e-03	-	5.03e-03	-	1.77e-02	-
	3	7.23e-04	2.30	9.67e-04	2.38	3.56e-03	2.31
	4	1.48e-04	2.29	1.95e-04	2.31	7.24e-04	2.30
	5	2.69e-05	2.46	3.51e-05	2.47	1.35e-04	2.43
$k = 2,$ $M = 4$	2	4.01e-03	-	5.05e-03	-	1.31e-02	-
	3	7.56e-04	2.41	9.89e-04	2.35	3.41e-03	1.95
	4	1.54e-04	2.29	1.96e-04	2.33	7.18e-04	2.25
	5	2.73e-05	2.50	3.52e-05	2.48	1.34e-04	2.42

Table 2: 2D Burgers' equation at $T = 0.01$, $\Delta t = 0.1h$, sparse grid DG, Lagrange interpolation with inner interpolation points.

poly degrees	N	L ¹ -error	order	L ² -error	order	L [∞] -error	order
$k = 1,$ $M = 1$	2	2.54e-01	-	3.17e-01	-	1.05e+00	-
	3	7.00e-02	1.86	9.36e-02	1.76	3.29e-01	1.67
	4	3.61e-02	0.96	4.90e-02	0.93	2.45e-01	0.42
	5	1.60e-02	1.17	2.18e-02	1.17	1.29e-01	0.93
	6	7.61e-03	1.07	1.02e-02	1.09	7.15e-02	0.85
	7	3.48e-03	1.13	4.71e-03	1.12	3.33e-02	1.10
$k = 1,$ $M = 2$	2	2.58e-01	-	3.18e-01	-	1.04e+00	-
	3	7.23e-02	1.83	9.59e-02	1.73	3.75e-01	1.47
	4	2.89e-02	1.32	4.07e-02	1.23	2.47e-01	0.60
	5	8.70e-03	1.73	1.21e-02	1.75	8.07e-02	1.61
	6	2.98e-03	1.55	4.21e-03	1.52	3.03e-02	1.41
	7	1.13e-03	1.40	1.61e-03	1.38	1.10e-02	1.46
$k = 2,$ $M = 2$	2	2.47e-01	-	4.31e-01	-	2.29e+00	-
	3	1.42e-01	0.79	2.50e-01	0.79	2.13e+00	0.11
	4	1.62e-02	3.14	2.61e-02	3.26	2.22e-01	3.26
	5	5.13e-02	-1.67	1.13e-01	-2.11	1.05e+00	-2.23
	6	1.38e+06	-24.68	4.53e+06	-25.26	1.12e+08	-26.67
	7	6.35e-02	-	9.42e-02	-	5.56e-01	-
$k = 2,$ $M = 3$	3	1.54e-02	2.05	2.42e-02	1.96	1.87e-01	1.57
	4	3.37e-03	2.19	4.78e-03	2.34	4.77e-02	1.97
	5	7.12e-04	2.24	1.03e-03	2.21	9.49e-03	2.33
	6	3.71e-04	0.94	6.44e-04	0.68	7.64e-03	0.31
	7	2.13e-03	-2.52	4.31e-03	-2.74	6.56e-02	-3.10

Table 3: 2D Burgers' equation at $T = 0.01$, $\Delta t = 0.1h$, sparse grid DG, Lagrange interpolation with interface interpolation points.

poly degrees	N	L ¹ -error	order	L ² -error	order	L [∞] -error	order
$k = 1,$ $M = 1$	2	2.55e-01	-	3.17e-01	-	1.04e+00	-
	3	6.99e-02	1.87	9.35e-02	1.76	3.28e-01	1.66
	4	3.58e-02	0.97	4.87e-02	0.94	2.45e-01	0.42
	5	1.58e-02	1.18	2.15e-02	1.18	1.27e-01	0.95
	6	7.47e-03	1.08	1.00e-02	1.10	7.05e-02	0.85
	7	3.40e-03	1.14	4.60e-03	1.13	3.30e-02	1.09
$k = 1,$ $M = 2$	2	2.60e-01	-	3.20e-01	-	1.01e+00	-
	3	6.60e-02	1.98	8.68e-02	1.88	3.18e-01	1.67
	4	2.84e-02	1.22	4.01e-02	1.12	2.38e-01	0.42
	5	8.14e-03	1.80	1.13e-02	1.83	7.49e-02	1.67
	6	2.70e-03	1.59	3.88e-03	1.54	2.73e-02	1.46
	7	8.07e-04	1.74	1.17e-03	1.73	1.10e-02	1.31
$k = 2,$ $M = 2$	2	5.63e-02	-	6.94e-02	-	1.52e-01	-
	3	2.85e-02	0.98	3.40e-02	1.03	8.23e-02	0.88
	4	5.74e-03	2.31	7.71e-03	2.14	2.79e-02	1.56
	5	2.68e-03	1.10	3.35e-03	1.20	1.05e-02	1.41
	6	6.14e-04	2.13	7.70e-04	2.12	3.51e-03	1.58
	7	1.59e-04	1.95	2.03e-04	1.92	1.21e-03	1.54
$k = 2,$ $M = 3$	2	6.35e-02	-	9.37e-02	-	5.51e-01	-
	3	1.53e-02	2.05	2.40e-02	1.97	1.84e-01	1.58
	4	3.37e-03	2.18	4.78e-03	2.33	4.72e-02	1.96
	5	7.09e-04	2.25	1.02e-03	2.22	9.25e-03	2.35
	6	3.49e-04	1.02	6.03e-04	0.77	7.12e-03	0.38
	7	1.70e-03	-2.29	3.44e-03	-2.51	5.21e-02	-2.87

Table 4: 2D Burgers' equation at $T = 0.01$, $\Delta t = 0.1h$ for $k = 1, 2$ and $\Delta t = 0.1h^{4/3}$ for $k = 3$, sparse grid DG, Hermite interpolation.

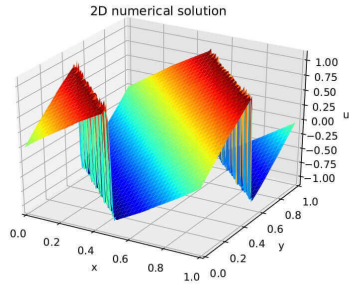
poly degrees	N	L ¹ -error	order	L ² -error	order	L [∞] -error	order
$k = 1,$ $M = 3$	2	2.56e-01	-	3.18e-01	-	1.04e+00	-
	3	6.57e-02	1.96	8.66e-02	1.88	3.26e-01	1.67
	4	2.86e-02	1.20	4.00e-02	1.11	2.27e-01	0.53
	5	8.30e-03	1.78	1.15e-02	1.80	7.36e-02	1.62
	6	2.85e-03	1.54	3.99e-03	1.52	2.59e-02	1.51
	7	8.81e-04	1.70	1.23e-03	1.70	1.03e-02	1.33
$k = 2,$ $M = 3$	2	7.65e-02	-	9.46e-02	-	1.90e-01	-
	3	2.87e-02	1.42	3.64e-02	1.38	8.94e-02	1.09
	4	4.15e-03	2.79	5.38e-03	2.76	1.63e-02	2.45
	5	1.42e-03	1.55	1.88e-03	1.51	6.32e-03	1.37
	6	1.60e-04	2.78	2.11e-04	2.80	9.04e-04	2.55
	7	2.75e-05	2.54	3.67e-05	2.52	2.23e-04	2.02
$k = 2,$ $M = 5$	2	5.23e-02	-	6.30e-02	-	1.58e-01	-
	3	8.69e-03	2.59	1.17e-02	2.42	3.90e-02	2.02
	4	2.91e-03	1.58	4.11e-03	1.52	1.80e-02	1.12
	5	3.85e-04	2.92	5.45e-04	2.91	3.07e-03	2.55
	6	8.18e-05	2.23	1.25e-04	2.12	1.12e-03	1.45
	7	1.37e-05	2.58	1.99e-05	2.65	2.26e-04	2.31
$k = 3,$ $M = 5$	2	3.73e-02	-	4.94e-02	-	1.15e-01	-
	3	5.23e-03	2.84	9.22e-03	2.42	3.89e-02	1.57
	4	4.27e-04	3.62	6.34e-04	3.86	2.03e-03	4.26
	5	4.37e-05	3.29	6.85e-05	3.21	2.86e-04	2.83
	6	3.75e-06	3.54	6.19e-06	3.47	6.26e-05	2.19
	7	2.81e-07	3.74	4.46e-07	3.80	3.16e-06	4.31

We run the simulations with a fixed maximum mesh level $N = 8$ and different ϵ values, and we report the L^2 errors and the number of active degrees of freedom at $T = 0.01$ in Table 5. We observe similar convergence rates as in Table 1 in [26]: R_ϵ is slightly smaller than 1, and R_{DoF} is much larger than $(k+1)/2$ (R_{DoF} for the standard adaptive DG scheme for 2D problems) but still smaller than $(k+1)$. This demonstrates the effectiveness of the multiresolution adaptive algorithm. Sparsity is indeed achieved for smooth solutions.

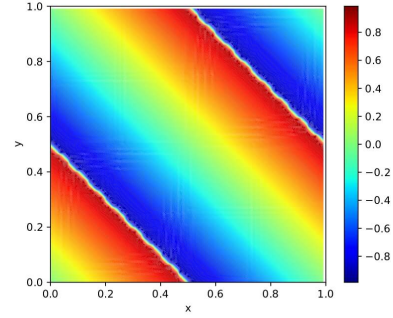
Table 5: 2D Burgers' equation at $T = 0.01$. Convergence rates with respect to the error threshold and degrees of freedom.

	ϵ	DoF	L^2 -error	R_{DoF}	R_ϵ
$k = 1$	1e-03	1104	2.36e-03	-	-
	5e-04	1584	1.33e-03	1.59	0.83
	1e-04	3488	3.89e-04	1.56	0.76
	5e-05	4608	2.95e-04	0.98	0.40
	1e-05	9408	9.29e-05	1.62	0.72
	5e-06	12272	4.79e-05	2.49	0.95
$k = 2$	1e-03	684	1.01e-03	-	-
	5e-04	792	6.72e-04	2.76	0.58
	1e-04	1656	2.02e-04	1.63	0.75
	5e-05	1908	1.20e-04	3.71	0.76
	1e-05	3600	3.83e-05	1.79	0.71
	5e-06	4068	2.33e-05	4.09	0.72
$k = 3$	1e-03	480	5.66e-04	-	-
	5e-04	608	1.49e-04	5.63	1.92
	1e-04	1152	5.52e-05	1.56	0.62
	5e-05	1472	2.49e-05	3.25	1.15
	1e-05	1920	1.16e-05	2.89	0.48
	5e-06	2624	5.62e-06	2.31	1.04

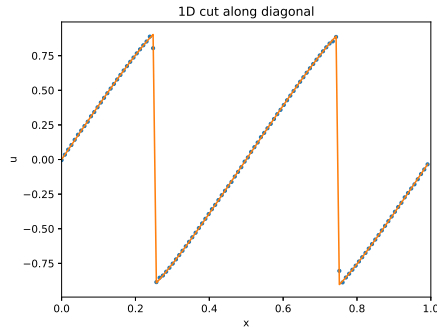
Finally, we test the ability of our scheme on capturing non-smooth solutions. We also take the same initial value. The shock begins to develop at $t = \frac{1}{4\pi} \approx 0.07958$. The numerical results at $t = 0.175$ are shown in Fig. 5. We observe the numerical solution coincides with the exact solution very well. The elements with non-zero artificial viscosity are also concentrated near the shock.



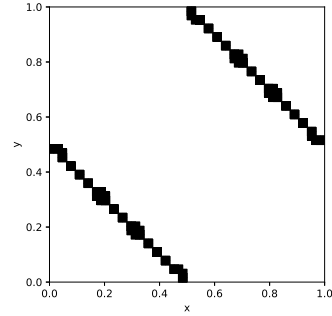
(a) numerical solution (surface plot)



(b) numerical solution (contour plot)



(c) numerical solution in 1D cut along diagonal



(d) elements with artificial viscosity

Figure 5: Example 4.3: 2D Burgers' equation at $t = 0.175$. $N = 7$ and $\epsilon = 5e - 4$. (a) numerical solution (surface plot); (b) numerical solution (contour plot); (c) numerical solution in 1D cut along diagonal; (d) elements with artificial viscosity.

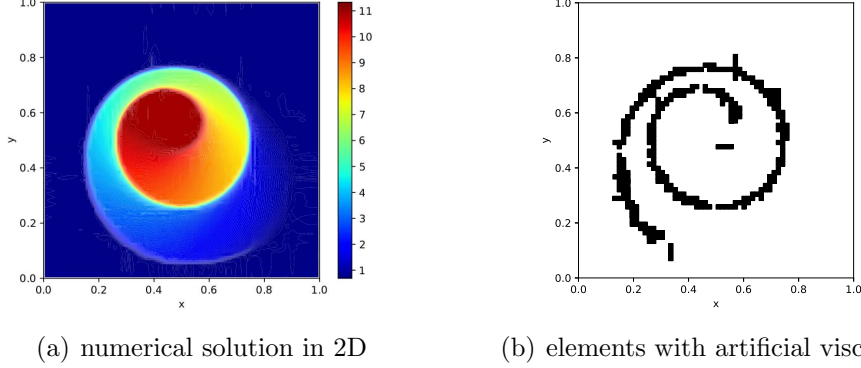


Figure 6: Example 4.4: 2D KPP rotating wave problem at $t = 0.2$. $N = 7$ and $\epsilon = 5e - 4$. Left: numerical solution in 2D; right: elements with artificial viscosity.

Example 4.4 (2D KPP rotating wave problem). *In the last example, we consider the 2D KPP rotating wave problem with the non-convex physical flux:*

$$u_t + \sin(u)_x + \cos(u)_y = 0.$$

The initial condition is

$$u_0(x, y) = \begin{cases} 3.5\pi, & (x - \frac{1}{2})^2 + (y - \frac{1}{2})^2 \leq \frac{1}{16}, \\ 0.25\pi, & \text{otherwise.} \end{cases}$$

This is a rather challenging test case, since a two-dimensional composite wave structure is present [24]. The code is run up to $t = 0.2$. The maximum mesh level is $N = 7$ and the error threshold is $\epsilon = 5 \times 10^{-4}$. The numerical solutions and elements with non-zero artificial viscosity are shown in Fig. 6. Our numerical scheme can capture the wave structure very well.

5 Concluding remarks

In this work, we propose an adaptive multiresolution DG scheme for scalar hyperbolic conservation laws in multidimensions. Besides the Alpert's multiwavelets, the interpolatory multiwavelets are applied to treat the nonlinear integrals over elements and edges in DG schemes. From numerical study, we

find that the multiresolution Hermite interpolation is the most stable. Because of the coherence of the multiresolution interpolation with the MRA of the numerical solution, our method can achieve similar computational complexity as the sparse grid DG method for smooth solutions [25, 26]. Artificial viscosity and adaptivity are activated for non-smooth solutions. The required DoF corresponds to the intrinsic complexity of the solution structure, and artificial viscosity is only added at locations near the shock maintaining sharpness of the solution profile.

We highlight some possible extensions to this work. The first is a detailed study of parameters in artificial viscosity. Some literature on the artificial viscosity for the standard DG may be helpful [37, 44]. The second is the extension to systems of conservation laws such as Euler equations of gas dynamics. We will also consider the application of the scheme to high-dimensional Hamilton-Jacobi equations.

Acknowledgements

We would like to thank Chi-Wang Shu from Brown University for providing the CFL constants of local DG method for diffusion equations and many fruitful discussions.

A Lagrange interpolation basis functions

For the completeness of our paper, we present the multiresolution interpolation basis functions, which are first introduced in [49]. In this part, we focus on the Lagrange interpolation, i.e. $K = 0$. The case in which the interpolation points are imposed in the inner domain, as implemented in Table 2 is discussed first, followed by the case in which the points are imposed at the cell interface, see the corresponding numerical results in Table 3.

The basis functions in \tilde{W}_1 are piecewise polynomials on $I_l := (0, \frac{1}{2})$ and $I_r := (\frac{1}{2}, 1)$. Note that the functions may be discontinuous at the interface $x = 1/2$, thus I_l and I_r are both defined to be open intervals. The basis functions in \tilde{W}_1 in this paper are all supported on one half interval I_l or I_r and vanish on the other half. For simplicity, we will only declare the function on its support. For example, $\psi_0(x)|_{I_r}$ gives the definition of ψ_0 on I_r and indicates that ψ_0 vanishes on I_l .

A.1 interpolation points in the inner domain

A.1.1 $P = 1$ and $K = 0$

The interpolation points are

$$\tilde{X}_0 = \{\frac{1}{3}, \frac{2}{3}\}, \quad \tilde{X}_1 = \{\frac{1}{6}, \frac{5}{6}\}.$$

The basis functions in \tilde{W}_0^1 and \tilde{W}_1^1 are

$$\begin{aligned} \phi_0(x) &= -3x + 2, & \phi_1(x) &= 3x - 1. \\ \psi_0(x)|_{I_l} &= -6x + 2, & \psi_1(x)|_{I_r} &= 6x - 4. \end{aligned}$$

A.1.2 $P = 2$ and $K = 0$

The interpolation points are

$$\tilde{X}_0 = \{\frac{1}{6}, \frac{1}{3}, \frac{2}{3}\}, \quad \tilde{X}_1 = \{\frac{1}{12}, \frac{7}{12}, \frac{5}{6}\}.$$

The basis functions in \tilde{W}_0^2 and \tilde{W}_1^2 are

$$\begin{aligned} \phi_0(x) &= \frac{4}{3}(3x - 2)(3x - 1), & \phi_1(x) &= -(3x - 2)(6x - 1), \\ \phi_2(x) &= \frac{1}{3}(3x - 1)(6x - 1). \end{aligned}$$

and

$$\begin{aligned} \psi_0(x)|_{I_l} &= \frac{8}{3}(3x - 1)(6x - 1), & \psi_1(x)|_{I_r} &= \frac{8}{3}(3x - 2)(6x - 5), \\ \psi_2(x)|_{I_r} &= \frac{2}{3}(3x - 2)(12x - 7). \end{aligned}$$

A.1.3 $P = 3$ and $K = 0$

The interpolation points are

$$\tilde{X}_0 = \{\frac{1}{5}, \frac{2}{5}, \frac{3}{5}, \frac{4}{5}\}, \quad \tilde{X}_1 = \{\frac{1}{10}, \frac{3}{10}, \frac{7}{10}, \frac{9}{10}\}.$$

The basis functions in \tilde{W}_0^3 and \tilde{W}_1^3 are

$$\begin{aligned} \phi_0(x) &= -\frac{1}{6}(5x - 4)(5x - 3)(5x - 2), & \phi_1(x) &= \frac{1}{2}(5x - 4)(5x - 3)(5x - 1), \\ \phi_2(x) &= -\frac{1}{2}(5x - 4)(5x - 2)(5x - 1), & \phi_3(x) &= \frac{1}{6}(5x - 3)(5x - 2)(5x - 1), \end{aligned}$$

and

$$\begin{aligned} \psi_0(x)|_{I_l} &= -\frac{2}{3}(5x - 2)(5x - 1)(10x - 3), \\ \psi_1(x)|_{I_l} &= -2(5x - 2)(5x - 1)(10x - 1), \\ \psi_2(x)|_{I_r} &= 2(5x - 4)(5x - 3)(10x - 9), \\ \psi_3(x)|_{I_r} &= \frac{2}{3}(5x - 4)(5x - 3)(10x - 7). \end{aligned}$$

A.2 interpolation points at the interface

A.2.1 $P = 1$ and $K = 0$

The interpolation points are

$$\tilde{X}_0 = \{0^+, 1^-\}, \quad \tilde{X}_1 = \{(\frac{1}{2})^-, (\frac{1}{2})^+\}.$$

Here and below, we use superscripts $+$, $-$ to emphasize the left and right limits of a function at that point. This is a feature of the discontinuous piecewise polynomial space.

The basis functions in \tilde{W}_0^1 and \tilde{W}_1^1 are

$$\begin{aligned} \phi_1(x) &= -x + 1, & \phi_2(x) &= x, \\ \psi_1(x)|_{I_l} &= 2x, & \psi_2(x)|_{I_r} &= -2x + 2. \end{aligned}$$

A.2.2 $P = 2$ and $K = 0$

The interpolation points are

$$\tilde{X}_0 = \{0^+, (\frac{1}{2})^-, 1^-\}, \quad \tilde{X}_1 = \{(\frac{1}{4})^-, (\frac{1}{2})^+, (\frac{3}{4})^-\}.$$

The basis functions in \tilde{W}_0^2 and \tilde{W}_1^2 are

$$\phi_1(x) = 2(x - \frac{1}{2})(x - 1), \quad \phi_2(x) = -4x(x - 1), \quad \phi_3(x) = 2x(x - \frac{1}{2}),$$

and

$$\begin{aligned} \psi_0(x)|_{I_l} &= -16x(x - \frac{1}{2}), & \psi_1(x)|_{I_r} &= 8(x - \frac{3}{4})(x - 1), \\ \psi_2(x)|_{I_r} &= -16(x - \frac{1}{2})(x - 1). \end{aligned}$$

A.2.3 $P = 3$ and $K = 0$

The interpolation points are

$$\tilde{X}_0 = \{0^+, (\frac{1}{4})^-, (\frac{1}{2})^-, 1^-\}, \quad \tilde{X}_1 = \{(\frac{1}{8})^-, (\frac{1}{2})^+, (\frac{5}{8})^-, (\frac{3}{4})^-\}.$$

The basis functions in \tilde{W}_0^3 and \tilde{W}_1^3 are

$$\begin{aligned} \phi_0(x) &= -(x - 1)(2x - 1)(4x - 1), & \phi_1(x) &= \frac{32}{3}x(x - 1)(2x - 1), \\ \phi_2(x) &= -4x(x - 1)(4x - 1), & \phi_3(x) &= \frac{1}{3}x(2x - 1)(4x - 1), \end{aligned}$$

and

$$\begin{aligned} \psi_0(x)|_{I_l} &= \frac{64}{3}x(2x - 1)(4x - 1), & \psi_1(x)|_{I_r} &= -2(x - 1)(4x - 3)(8x - 5), \\ \psi_2(x)|_{I_r} &= \frac{64}{3}(x - 1)(2x - 1)(4x - 3), & \psi_3(x)|_{I_r} &= -8(x - 1)(2x - 1)(8x - 5). \end{aligned}$$

B Hermite interpolation basis functions

The Hermite interpolation basis functions are presented here. The interpolation points are put at the cell interface:

$$\tilde{X}_0 = \{0^+, 1^-\}, \quad \tilde{X}_1 = \{(\frac{1}{2})^-, (\frac{1}{2})^+\}.$$

B.1 $P = 1$ and $K = 1$

The basis functions in \tilde{W}_0^3 and \tilde{W}_1^3 are

$$\begin{aligned} \phi_{0,0}(x) &= (x-1)^2(2x+1), & \phi_{1,0}(x) &= -x^2(2x-3), \\ \phi_{0,1}(x) &= x(x-1)^2, & \phi_{1,1}(x) &= x^2(x-1). \end{aligned}$$

and

$$\begin{aligned} \psi_{0,0}(x)|_{I_l} &= -4x^2(4x-3), & \psi_{1,0}(x)|_{I_r} &= 4(x-1)^2(4x-1), \\ \psi_{0,1}(x)|_{I_l} &= 2x^2(2x-1), & \psi_{1,1}(x)|_{I_r} &= 2(x-1)^2(2x-1), \end{aligned}$$

B.2 $P = 1$ and $K = 2$

The basis functions in \tilde{W}_0^5 and \tilde{W}_1^5 are

$$\begin{aligned} \phi_{0,0}(x) &= -(x-1)^3(6x^2+3x+1), & \phi_{0,1}(x) &= -x(x-1)^3(3x+1), \\ \phi_{0,2}(x) &= -\frac{1}{2}x^2(x-1)^3, & \phi_{1,0}(x) &= x^3(6x^2-15x+10), \\ \phi_{1,1}(x) &= -x^3(x-1)(3x-4), & \phi_{1,2}(x) &= \frac{1}{2}x^3(x-1)^2. \end{aligned}$$

and

$$\begin{aligned} \psi_{0,0}(x)|_{I_l} &= 16x^3(12x^2-15x+5), & \psi_{1,0}(x)|_{I_r} &= -16(x-1)^3(12x^2-9x+2), \\ \psi_{0,1}(x)|_{I_l} &= -8x^3(2x-1)(3x-2), & \psi_{1,1}(x)|_{I_r} &= -8(x-1)^3(2x-1)(3x-1), \\ \psi_{0,2}(x)|_{I_l} &= x^3(2x-1)^2, & \psi_{1,2}(x)|_{I_r} &= -(x-1)^3(2x-1)^2. \end{aligned}$$

References

- [1] S. ADJERID, K. D. DEVINE, J. E. FLAHERTY, AND L. KRIVODONOVA, *A posteriori error estimation for discontinuous Galerkin solutions of hyperbolic problems*, Computer Methods in Applied Mechanics and Engineering, 191 (2002), pp. 1097–1112.
- [2] B. ALPERT, G. BEYLKIN, D. GINES, AND L. VOZVOI, *Adaptive solution of partial differential equations in multiwavelet bases*, J. Comput. Phys., 182 (2002), pp. 149–190.
- [3] B. K. ALPERT, *A class of bases in L^2 for the sparse representation of integral operators*, SIAM Journal on Mathematical Analysis, 24 (1993), pp. 246–262.
- [4] M. A. ALVES, P. CRUZ, A. MENDES, F. D. MAGALHÃES, F. T. PINHO, AND P. J. OLIVEIRA, *Adaptive multiresolution approach for solution of hyperbolic PDEs*, Computer Methods in Applied Mechanics and Engineering, 191 (2002), pp. 3909–3928.
- [5] R. ARCHIBALD, G. FANN, AND W. SHELTON, *Adaptive discontinuous Galerkin methods in multiwavelets bases*, Applied Numerical Mathematics, 61 (2011), pp. 879–890.
- [6] F. BASSI AND S. REBAY, *Accurate 2D Euler computations by means of a high order discontinuous finite element method*, in Fourteenth International Conference on Numerical Methods in Fluid Dynamics, Springer, 1995, pp. 234–240.
- [7] K. S. BEY AND J. T. ODEN, *hp-version discontinuous Galerkin methods for hyperbolic conservation laws*, Computer Methods in Applied Mechanics and Engineering, 133 (1996), pp. 259–286.
- [8] B. BIHARI AND A. HARTEN, *Multiresolution schemes for the numerical solution of 2-D conservation laws I*, SIAM Journal on Scientific Computing, 18 (1997), pp. 315–354.
- [9] R. BISWAS, K. D. DEVINE, AND J. E. FLAHERTY, *Parallel, adaptive finite element methods for conservation laws*, Applied Numerical Mathematics, 14 (1994), pp. 255–283.

- [10] H.-J. BUNGARTZ AND M. GRIEBEL, *Sparse Grids*, Acta Numerica, 13 (2004), pp. 147–269.
- [11] J. L. D. CALLE, P. R. B. DEVLOO, AND S. M. GOMES, *Wavelets and adaptive grids for the discontinuous Galerkin method*, Numerical Algorithms, 39 (2005), pp. 143–154.
- [12] G. CHIAVASSA, R. DONAT, AND S. MÜLLER, *Multiresolution-based adaptive schemes for hyperbolic conservation laws*, in Adaptive Mesh Refinement-Theory and Applications, Springer, 2005, pp. 137–159.
- [13] B. COCKBURN, S. HOU, AND C.-W. SHU, *The Runge-Kutta local projection discontinuous Galerkin finite element method for conservation laws. IV. The multidimensional case*, Mathematics of Computation, 54 (1990), pp. 545–581.
- [14] B. COCKBURN, G. E. KARNIADAKIS, AND C.-W. SHU, *The development of discontinuous Galerkin methods*, in Discontinuous Galerkin Methods, Springer, 2000, pp. 3–50.
- [15] B. COCKBURN AND C.-W. SHU, *TVB Runge-Kutta local projection discontinuous galerkin finite element method for conservation laws. II. General framework*, Mathematics of computation, 52 (1989), pp. 411–435.
- [16] B. COCKBURN AND C.-W. SHU, *Runge-Kutta discontinuous Galerkin methods for convection-dominated problems*, Journal of Scientific Computing, 16 (2001), pp. 173–261.
- [17] A. COHEN, S. KABER, S. MÜLLER, AND M. POSTEL, *Fully adaptive multiresolution finite volume schemes for conservation laws*, Mathematics of Computation, 72 (2003), pp. 183–225.
- [18] W. DAHMEN, B. GOTTSCHLICH-MÜLLER, AND S. MÜLLER, *Multiresolution schemes for conservation laws*, Numerische Mathematik, 88 (2001), pp. 399–443.
- [19] N. DISCACCIATI, J. S. HESTHAVEN, AND D. RAY, *Controlling oscillations in high-order discontinuous Galerkin schemes using artificial viscosity tuned by neural networks*, tech. report, 2019.

- [20] N. GERHARD, D. CAVIEDES-VOULLIÈME, S. MÜLLER, AND G. KESSERWANI, *Multiwavelet-based grid adaptation with discontinuous Galerkin schemes for shallow water equations*, Journal of Computational Physics, 301 (2015), pp. 265–288.
- [21] N. GERHARD, F. IACONO, G. MAY, S. MÜLLER, AND R. SCHÄFER, *A high-order discontinuous Galerkin discretization with multiwavelet-based grid adaptation for compressible flows*, Journal of Scientific Computing, 62 (2015), pp. 25–52.
- [22] N. GERHARD AND S. MÜLLER, *Adaptive multiresolution discontinuous Galerkin schemes for conservation laws: multi-dimensional case*, Computational and Applied Mathematics, 35 (2016), pp. 321–349.
- [23] M. GRIEBEL AND G. ZUMBUSCH, *Adaptive sparse grids for hyperbolic conservation laws*, in Hyperbolic problems: theory, numerics, applications, Springer, 1999, pp. 411–422.
- [24] J.-L. GUERMOND, R. PASQUETTI, AND B. POPOV, *Entropy viscosity method for nonlinear conservation laws*, Journal of Computational Physics, 230 (2011), pp. 4248–4267.
- [25] W. GUO AND Y. CHENG, *A sparse grid discontinuous Galerkin method for high-dimensional transport equations and its application to kinetic simulations*, SIAM Journal on Scientific Computing, 38 (2016), pp. A3381–A3409.
- [26] W. GUO AND Y. CHENG, *An adaptive multiresolution discontinuous Galerkin method for time-dependent transport equations in multidimensions*, SIAM Journal on Scientific Computing, 39 (2017), pp. A2962–A2992.
- [27] T. HAGSTROM AND D. APPELÖ, *Solving PDEs with hermite interpolation*, in Spectral and High Order Methods for Partial Differential Equations ICOSAHOM 2014, Springer, 2015, pp. 31–49.
- [28] A. HARTEN, *Multiresolution algorithms for the numerical solution of hyperbolic conservation laws*, Communications on Pure and Applied Mathematics, 48 (1995), pp. 1305–1342.

- [29] R. HARTMANN AND P. HOUSTON, *Adaptive discontinuous Galerkin finite element methods for the compressible Euler equations*, Journal of Computational Physics, 183 (2002), pp. 508–532.
- [30] R. HARTMANN AND P. HOUSTON, *Adaptive discontinuous Galerkin finite element methods for nonlinear hyperbolic conservation laws*, SIAM Journal on Scientific Computing, 24 (2003), pp. 979–1004.
- [31] J. HESTHAVEN AND T. WARBURTON, *Nodal discontinuous Galerkin methods: algorithms, analysis, and applications*, vol. 54, Springer, 2007.
- [32] P. HOUSTON, B. SENIOR, AND E. SÜLI, *hp-Discontinuous Galerkin finite element methods for hyperbolic problems: error analysis and adaptivity*, International Journal for Numerical Methods in Fluids, 40 (2002), pp. 153–169.
- [33] N. HOVHANNISYAN, S. MÜLLER, AND R. SCHÄFER, *Adaptive multiresolution discontinuous Galerkin schemes for conservation laws*, Mathematics of Computation, 83 (2014), pp. 113–151.
- [34] J. HUANG AND C.-W. SHU, *Error estimates to smooth solutions of semi-discrete discontinuous Galerkin methods with quadrature rules for scalar conservation laws*, Numerical Methods for Partial Differential Equations, 33 (2017), pp. 467–488.
- [35] F. IACONO, G. MAY, S. MÜLLER, AND R. SCHÄFER, *An adaptive multiwavelet-based DG discretization for compressible fluid flow*, in Computational Fluid Dynamics 2010, Springer, 2011, pp. 813–820.
- [36] G. KESSERWANI, D. CAVIEDES-VOULLIEME, N. GERHARD, AND S. MÜLLER, *Multiwavelet discontinuous Galerkin h-adaptive shallow water model*, Computer Methods in Applied Mechanics and Engineering, 294 (2015), pp. 56–71.
- [37] A. KLÖCKNER, T. WARBURTON, AND J. S. HESTHAVEN, *Viscous shock capturing in a time-explicit discontinuous Galerkin method*, Mathematical Modelling of Natural Phenomena, 6 (2011), pp. 57–83.
- [38] A. KORNELUS AND D. APPELÖ, *On the scaling of entropy viscosity in high order methods*, in Spectral and High Order Methods for Partial Differential Equations ICOSAHOM 2016, Springer, 2017, pp. 175–187.

- [39] B. LASTDRAGER, B. KOREN, AND J. VERWER, *The sparse-grid combination technique applied to time-dependent advection problems*, Applied numerical mathematics, 38 (2001), pp. 377–401.
- [40] Y. LIU, Y. CHENG, S. CHEN, AND Y.-T. ZHANG, *Krylov implicit integration factor discontinuous Galerkin methods on sparse grids for high dimensional reaction-diffusion equations*, Journal of Computational Physics, (2019).
- [41] L. PARESCHI AND G. RUSSO, *Implicit–explicit Runge–Kutta schemes and applications to hyperbolic systems with relaxation*, Journal of Scientific Computing, 25 (2005), pp. 129–155.
- [42] P.-O. PERSSON AND J. PERAIRE, *Sub-cell shock capturing for discontinuous Galerkin methods*, in 44th AIAA Aerospace Sciences Meeting and Exhibit, 2006, p. 112.
- [43] J. QIU AND C.-W. SHU, *Runge–kutta discontinuous Galerkin method using WENO limiters*, SIAM Journal on Scientific Computing, 26 (2005), pp. 907–929.
- [44] D. RAY AND J. S. HESTHAVEN, *An artificial neural network as a troubled-cell indicator*, Journal of Computational Physics, 367 (2018), pp. 166–191.
- [45] J.-F. REMACLE, J. E. FLAHERTY, AND M. S. SHEPHARD, *An adaptive discontinuous Galerkin technique with an orthogonal basis applied to compressible flow problems*, SIAM Review, 45 (2003), pp. 53–72.
- [46] J. SHEN AND H. YU, *Efficient spectral sparse grid methods and applications to high-dimensional elliptic problems*, SIAM J. Sci. Comput., 32 (2010), pp. 3228–3250.
- [47] C.-W. SHU AND S. OSHER, *Efficient implementation of essentially non-oscillatory shock-capturing schemes*, Journal of Computational Physics, 77 (1988), pp. 439–471.
- [48] Z. TAO, W. GUO, AND Y. CHENG, *Sparse grid discontinuous Galerkin methods for the Vlasov-Maxwell system*, arXiv preprint arXiv:1805.10747, (2018).

- [49] Z. TAO, Y. JIANG, AND Y. CHENG, *An adaptive high-order piecewise polynomial based sparse grid collocation method with applications*, (preprint).
- [50] M. VUIK AND J. RYAN, *Multiwavelet troubled-cell indicator for discontinuity detection of discontinuous Galerkin schemes*, J. Comput. Phys., 270 (2014), pp. 138–160.
- [51] Z. WANG, Q. TANG, W. GUO, AND Y. CHENG, *Sparse grid discontinuous Galerkin methods for high-dimensional elliptic equations*, Journal of Computational Physics, 314 (2016), pp. 244–263.